Satisfactory catalyst stability in SNG production using real biogas despite sulfur poisoning evidences at different reactor zones

Jordi Guilera[a*], Rodrigo Soto[b], Andreina Alarcón[a,c] and Teresa Andreu[d]

[a]Catalonia Institute for Energy Research (IREC), Jardins de les Dones de Negre 1, 08930 Sant Adrià de Besòs, Spain

[b]Synthesis and Solid State Pharmaceutical Centre (SSPC), Bernal Institute, Department of Chemical and Environmental Science, University of Limerick. Limerick V94 T9PX, Ireland.

[c]Escuela Superior Politécnica del Litoral (ESPOL), Facultad de Ingeniería en Ciencias de la Tierra, Campus Gustavo Galindo Km.30.5 Vía Perimetral, P.O. Box 09-01-5863, Guayaquil, Ecuador.

[d]Departament de Ciència de Materials i Química Física, Universitat de Barcelona, Martí i Franquès, 1, Barcelona 08028, Spain

*corresponding author: jguilera@irec.cat

Abstract

The performance of a nickel-ceria micro-catalyst in biogas methanation was evaluated in a complete pilot plant during 1,000 hours. The core of the exothermic methanation process consisted in two micro-reactors using a decreasing temperature profile, intermediate water removal and moderate pressure. The obtained gas quality and the reactors temperature profile remained constant during operation, indicating no signs of catalyst deactivation. After the experimental campaign, catalyst samples from different reactors sections were withdrawn, collected and independently characterized. It has been demonstrated that the different reaction conditions, in which the catalyst operated, played a significant role on the different level of degradation of the catalyst samples. On one hand, various characterization techniques agreed that sintering of nickel and ceria nanoparticles (+10-30%) and loss of surface area (-20%) was restricted to the initial reactor zones, which is attributed to the higher operation temperatures. On the other hand, despite the cautions undertaken for biogas cleaning and gas monitoring, sulfur was detected along the entire reactor longitudinal profile (0.25-0.91%). Accordingly, a progressive diffuse flow poisoning mechanism is expected from very long operation times. In particular, higher amount of sulfur was detected in the latest reactor zones, which operated at lower temperatures and under more oxidizing conditions. Beneficially, sulfur was predominantly detected as Ce_2O_2S phase, confirming thereby the crucial sacrificial role of CeO_2 that allows for maintaining the catalytic activity of nickel active sites. The overall outcome of this work is very promising and reveals a sufficient catalyst lifespan for industrial application.

Keywords: Synthetic natural gas; biogas methanation; CO_2 conversion; catalyst stability; poisoning

1. Introduction

Power to Gas relies on the conversion of renewable electricity into the so-called green hydrogen by water electrolysis [1]. The utilization of green hydrogen as energy vector has several benefits: it offers ways to decarbonize a broad range of sectors and enables renewables to provide a greater contribution in the electricity supply system. However, hydrogen storage, transport, distribution and utilization in pure form still present certain technical limitations [2–4]. A plausible approach to circumvent such constraints is to further convert the hydrogen into hydrogen-based fuels. In this aspect, a simple way to supply hydrogen to customers is in the form of synthetic methane by its combination with carbon dioxide by means of the well-known Sabatier reaction. Obviously, this approach is also extremely appealing from an environmental standpoint since it entails the valorization of carbon dioxide, contributing therefore to mitigate the undesired impact of this greenhouse gas. Synthetic methane is known as synthetic natural gas due to its similar chemical composition [5,6]. Among different synthetic fuels [7], synthetic natural gas presents the outstanding advantage of an already available gas infrastructure for both producers and consumers. Biogas, composed of about 65% CH_4 and 35% CO_2, is the most suitable carbon feedstock to produce synthetic natural gas because a considerable amount of methane is already present in the feed. In this sense, the amount of methane is 3-fold higher than using pure CO_2, with its positive impact on cost-benefit analysis [8]. In addition, this reaction pathway offers the possibility of complete utilization of renewable carbon from biogas [9].

The thermo-chemical conversion of biogas to synthetic natural gas can be carried out using a nickel-based heterogeneous catalyst at moderate temperature (250-500 ºC) and pressure (5-20 bar). Comprehensive advances in catalyst research for CO_2 methanation can be found in recent reviews [10,11]. Most of the studies deal with the initial catalytic activity, whereas detailed studies on catalyst deactivation are less frequent despite its paramount importance towards industrial application. The classical causes of catalyst deactivation are namely chemical, mechanical and thermal [12]. In the present reaction system, sintering of nickel particles, structural changes of the support, re-oxidation of metal induced by changes of the reaction atmosphere, modification of the surface adsorption capacity and hydroxide formation at low temperature have been reported as the main causes of smooth [13–17] or even negligible catalyst deactivation [18,19]. In contrast, catalyst poisoning by sulfur derivatives, e.g. H_2S, can have devastating effects on the reactor performance [20,21].

The first obvious action to prevent catalyst poisoning is by an adequate biogas purification. Conventional biogas treatments using specific activated carbon can reduce H_2S content to 1 ppm [21]; enough for the current biogas applications in heat, electricity generation and upgrading to biomethane [22]. However, nickel-based methanation catalysts are much more sensitive to sulfur poisoning, even up to few ppb [23], especially at low reaction temperatures

[24]. In this sense, an additional sulfur guard filter needs to be included in methanation plants; for instance, metal oxide-based absorbents [25,26]. Complete sulfur removal at biogas sites is still a technological challenge for both the purification [27] as well as for the analytical capability [28]. A second action to extend the catalyst lifetime is by incorporating a sacrificial agent. Promoted catalysts show superior resistance towards H_2S poisoning, which was recently correlated to sulfur adsorption on promoter phases [29,30], protecting thereby the Ni active sites. In our previous work at laboratory isothermal conditions, the mechanism by which Ce-promoted catalyst renders an enhanced tolerance was unraveled [31]. A third action to lengthen the progressive deactivation of the catalyst consists of loading the reactor with extra catalyst [32,33], leading to constant activity as long as excess catalyst is available to ensure that chemical equilibrium at the outlet temperature is still reached [34].

The methanation process can be successfully operated using industrial biogas provided that some of the aforementioned precautions are considered [35]. Literature on demo or industrial plant operation using real feedstock is very scarce. Interestingly, Dannesboe et al. demonstrated successful removal of H_2S by KI impregnated alkaline activated carbon by feeding oxygen and using a ZnO sulfur guard filter. After 1000 hours of continuous operation, they claimed that the methanation technology outperforms the lifetime of most other plant components [36]. Recently, Gaikwad et al. reported a 4-stage fixed-bed reactor system with no sign of catalyst deactivation or activity loss during 500 h of operation [37]. Surprisingly, the collected and characterized catalyst samples revealed that Ni_3S_2 phase was formed on the catalyst, indicating sulfur contamination and a loss of almost half of the initial surface area. The spent catalyst was analyzed as an entire bulk without assessing the effects of the operating conditions. They recommended to implement a sacrificial ZnO filter before reaction and further investigation to better understand the catalyst degradation without apparent activity loss.

In the present work, we studied the stability of a CeO_2-promoted nickel micro-catalyst for 1,000 hours of operation in a two-step biogas methanation plant at industrially relevant conditions.

The catalyst worked at different temperatures and gas composition over the length of the reactors to achieve the desired synthetic natural gas quality. After the on-site test campaign, catalyst samples from different reactors sections were discharged, collected and comprehensively characterized. Within this novel strategy, relations between different operational conditions and catalyst physiochemical modifications are hereby disclosed.

2. Experimental

The biogas methanation pilot plant was located at the premises of EDAR Riu Sec (Sabadell, Spain), which processes the municipal waste water. The plant operates two anaerobic digesters (100 Nm^3/h) for treatment of primary and secondary slurry. A detailed description of the pilot plant can be found elsewhere [38].

2.1. Gas conditioning

The carbon source was obtained from anaerobic digestion, consisting mainly of methane and carbon dioxide. The hydrogen source was obtained from water electrolysis. Both streams were conditioned before entering the methanation process. The Process Flow Diagram of the gas conditioning is illustrated in Figure *1*. Raw biogas was obtained from anaerobic digestion of municipal sewage sludge at mesophilic conditions (1). Then, biogas was dried, cleaned and compressed, as described below. The stream was dried using a counter current water-glycol mixture at 5 ºC (2), then the biogas was driven by a blower (3) to the carbon filters. The first filter was composed of active carbon (Filtracar® EX64, CPL) to remove siloxanes and COV (4) and then, the filtered gas stream was compressed up to 10-15 bar (5). Most of the gas was directed towards a biogas upgrading plant to biomethane (50 Nm^3/h), while a small part to the methanation process (4 Nm^3/h). Before methanation, biogas was directed to a second active carbon filter (6), specially doped with KOH and KI for desulphurization of gases (Airlpel® Ultra DS, Desotec). Finally, biogas was impelled to a third filter (7), operated at 250 ºC and filled with ZnO-based adsorbent (ActiSorb®S2, Clariant). A particle filter was installed before gas mixing (8) and across other parts of the conditioning process, which are not detailed for simplicity.

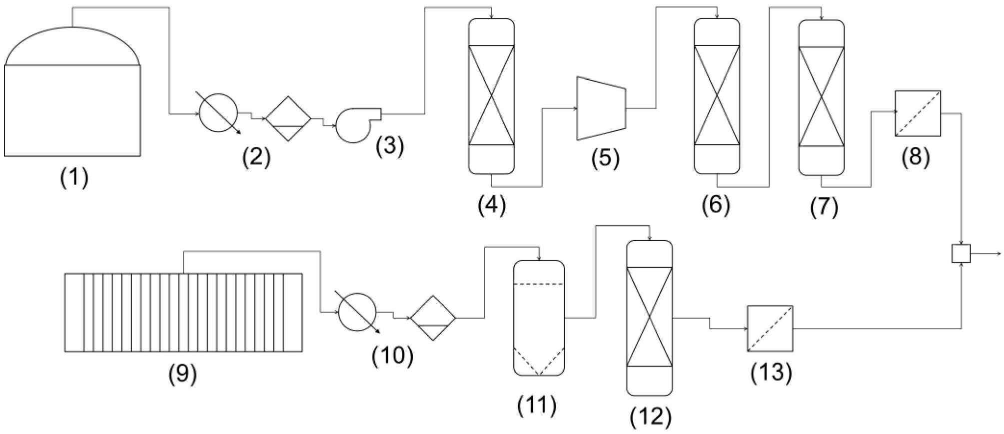

Figure *1*. Process flow diagram of biogas and hydrogen pre-treatment. (1) Anaerobic digester, (2) biogas dryer, (3) blower, (4) carbon filter, (5) compressor, (6) carbon filter, (7) ZnO filter, (8) particle filter, (9) electrolyzer, (10) hydrogen dryer, (11) coalescing filter, (12) silica gel filter, and (13) particle filter.

After conditioning, biogas samples were collected in sampling bags and pressurized cylinders and completely characterized by external analytic services according to standard biogas procedures [39]. Permanent gases, light hydrocarbons, sulfur compounds, volatile organic compounds (VOC), halogenated organic compounds (AOX), siloxanes and ammonia were comprehensively analyzed. A representative biogas composition after conditioning is summarized in Table *1*, as an average of three independent external analytics. The gas mixture consisted mainly by CH_4 (55.00%), CO_2 (44.63%), and other permanent gases found in much smaller quantity: N_2 (0.19%), H_2 (0.03%) and O_2 (0.03%). The main impurities consisted of VOCs and siloxanes, while ammonia and AOX were not detected. Specifically, VOCs detected were 2-propanol (1.6 mg/Nm^3), 2,2,4-trimethylpentane (0.8 mg/Nm^3), p-isopropyltoluene (0.2 mg/Nm^3); and the siloxanes found were hexamethylciclotrisiloxane (0.30 mg/Nm^3), octamethyltrisiloxane (0.18 mg/Nm^3), dodecamethylpentasiloxane (0.08 mg/Nm^3)

and decamethylciclopentasiloxane (0.033 mg/Nm^3). Special attention was paid to sulfur compounds and 13 different sulphur compounds (organic and inorganic) were analyzed by gas chromatography and sulfur chemiluminescence detector (SCD, Agilent 355). None of them was detected during the analyses. In this aspect, H_2S was below the detection limit 0.03 mg/Nm^3 (22 ppb), at least, during gas sampling.

Table *1*. Biogas composition after conditioning.

component	biogas (%)
CH_4	55.00
CO_2	44.63
N_2	0.19
H_2	0.03
O_2	0.03
impurities	mg/Nm^3
VOC	2.60
siloxanes	0.60
sulphur	ND
NH_3	ND
AOX	ND

As for hydrogen conditioning, an alkaline electrolyzer produced 6-10 bar of hydrogen on-site (G10, Erredue) (9). Hydrogen stream was cooled down by process water at T=10-30 ºC (10). At this point, hydrogen moisture was too high (≤ 2,000 ppm H_2O), especially in this case for the operation of the mass flow controllers. Thus, the stream was further passed through a 0.1 µm PVDF coalescing filter (25-64-7CK, Classic Filter) (11), an adsorption fixed-bed of silica gel drying granules (Chameleon®, VWR) (12) and finally through a particle filter (13). The composition of the hydrogen delivered to the methanation unit consisted of H_2 (≥99.5%) and some residual O_2 (≤0.5%). The introduction of oxygen into the reactor should be kept at minimum because its recombination with hydrogen is negative for the methanation process.

2.2. Methanation process

The methanation process was designed to convert up to 6 Nm^3/h of hydrogen to 1.5 Nm^3/h of synthetic gas (Equation 1). After hydrogen supply, biogas flow was adjusted according to the stoichiometry of the reaction. As illustrated in Figure *2*, the methanation process consisted of a 2-step synthesis unit, both including gas pre-heating, catalytic reaction and water condensation with subsequent separation.

$$CO_2 + 4H_2 \leftrightarrow CH_4 + 2H_2O \qquad \text{(Equation 1)}$$

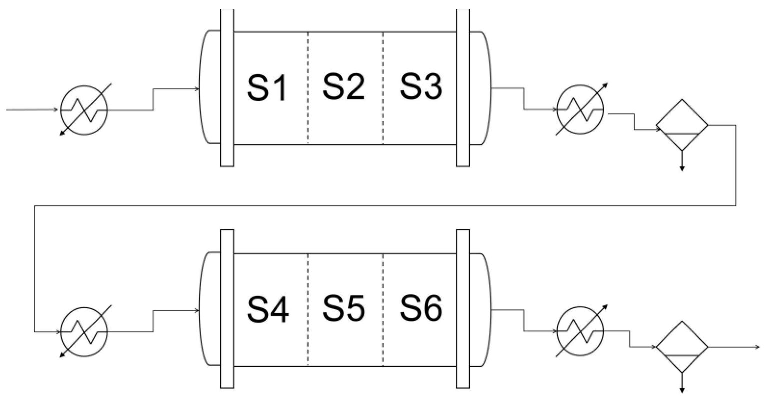

Figure *2*. Process flow diagram of the methanation process. S1-S6: reactors sections from which catalyst samples were withdrawn.

The thermo-catalytic reaction was carried out through a combination of micro-structured fixed bed reactors (INERATEC GmbH) and micro-size catalyst (IREC). Two micro-structured reactors in series were implemented, which were build on staking sequences of catalytic micro-beds and cooling foils. Details, claims and drawings of the reactor technology can be found in the patent WO2017211864A1 [40]. In the present device, the reaction volume of each reactor was 100 mL, formed by ten diffusion bonded reaction foils containing micro-pillars of 10 cm length. The first reactor was cooled down by vaporizing boiling water at high pressures ($P \leq 29$ bar·g) and the second by compressed air. Temperature inside the reactors was monitored in detail by 15 thermocouples. The represented temperatures consist of an average of the registered temperatures at each section.

The methanation plant operated for 2,000 hours using the same catalyst load. Within this period, a first set of exploratory experiments (1,000 hours) was performed to set the limits of the process, both in steady and non-steady state conditions. Further details on discontinuous experimental results on process intensification can be found in a previous work [41]. In very brief, the process can produce the desired gas quality at the gas hourly space velocity (GHSV) of 37,500 h^{-1}, at 5 bar·g and after 8 minutes after the start-up.

The second set of experiments consisted on 1,000 hours of continuous operation under remote control. This experimental campaign was devoted to study the autonomous operability of the plant and to evaluate the catalyst stability. The long-term continuous experiment was performed at fixed conditions. The electrolyzer worked at 30% of capacity at a flowrate of 1.5 Nm^3/h of hydrogen. Biogas was adjusted to the electrolyzer capacity at 0.375 Nm^3/h of carbon dioxide. Production of synthetic natural gas was around 1.22 Nm^3/h and the process pressure was set to 5 bar·g. At this low plant capacity, water-cooling of the first reactor was very soft (~5%), while the cooling of the second reactor was even unnecessary due to heat transfer to the environment [42]. CO_2 methanation reaction gases were sampled by a multi-port valve and analysed by an on-line gas micro-chromatograph (490 Agilent Technologies), which consisted of a dual channel cabinet including a 10m MS5A plot column (Argon) and a 10m Poraplot-U column (Helium). H_2S detection limit was 3 ppm. During the continuous operation, biogas flow was continuously adjusted to maintain the gas quality requirements for grid injection at the process outlet (≥92.5% CH_4, ≤5% H_2 and ≤2.5% CO_2).

2.3. Catalyst

The catalyst load used in this study was composed by 25 wt.% of nickel and 20 wt.% of CeO_2 supported on alumina [43]. The catalyst was prepared by wet impregnation method using γ-Al_2O_3 microspheres (Accu® Spheres SA62240 d_p=450-500 μm, Saint-Gobain NorPro), and salt precursors of nickel (II) nitrate hexahydrate [$Ni(NO_3)_2 6H_2O$] (98% purity, Alfa Aesar) and cerium (III) nitrate hexahydrate [$Ce(NO_3)_3 6H_2O$] (99% purity, Fluka). An aqueous solution of salt precursors was incorporated to dry alumina and mixed in a rotary vacuum evaporator for 1 h. At that point, the aqueous phase was evaporated at 85 ºC and 0.8 bar for 6 h. Later, the material was dried and calcined at 450 ºC for 30 min (1 ºC·min^{-1}). The first reactor was filled with 45 g of catalyst (d_p=400-500 μm) and diluted with 75 g of silicon carbide (d_p=300-400 μm), and the second reactor with 60 g of catalyst and 50 g of diluent. The catalyst was reduced in-situ with diluted hydrogen (5% H_2/Ar, Linde). The activation procedure started by a heating ramp (1.2 ºC·min^{-1}, 800 NL·h^{-1}) up to 480 ºC. Afterwards, the temperature was kept constant for 3 h (1,200 NL·h^{-1}) and then was decreased to 320 ºC (6 ºC·min^{-1}, 800 NL·h^{-1}). The reduction process lasted for about 10 h. During catalyst activation, the pressure was set to 5 bar·g and the total gas consumption was about 9 Nm^3.

2.4. Material characterization

After operation, the reactors were dismantled and the catalyst discharged for characterization. During the discharge, the catalyst from the different sections was collected as separated samples (S1-S6) related to their position inside the reactors, as illustrated in Figure 2. The analysis of fresh and spent catalyst samples consisted of N_2-physisorption, X-ray diffraction (XRD), scanning electron microscopy – energy-dispersive X-ray spectroscopy (SEM-EDX), transmission electron microscopy (TEM), high-resolution TEM (HRTEM) and attenuated total reflectance-Fourier transform infrared spectroscopy (ATR- FTIR). The fresh sample was characterized after reduction, using 100 NmL·min^{-1} in a 5 vol.% H_2/Ar flow at 500 °C for 3 h with a heating and cooling ramp of 1 °C·min^{-1}.

N_2-physisorption (adsorption/desorption) measurements were determined at liquid nitrogen temperature using an automated TriStar II 3020-Micromeritics analyzer. Samples were degassed at 90 °C for 1 h, and then at 250 °C for 4 h in a FlowPrep 060-Micromeritics. Brunauer-Emmett-Teller (BET) method was used to calculate the BET surface area for a relative pressure (P·P$_o^{-1}$) range of 0.05-0.30. Barrett-Joyner-Halenda (BJH) method was applied to desorption branch of the isotherms to determine the average pore size and the total pore volume, which was calculated from the maximum adsorption value at $P \cdot P_o^{-1}$ = 0.999.

XRD patterns were collected within the 2ϴ range 20-80° in a Bruker type XRD D8 Advance A25 diffractometer using a Cu Kα radiation (λ = 1.5406 Å), a voltage of 40 kV, a current of 40 mA and a step size of 0.05° (with 3 s duration at each step). The average crystal sizes of the metallic nickel (Ni^0) and cerium oxide (CeO_2) were estimated using the Scherrer's equation at the most intense peaks; 2ϴ=44.50º for Ni (111) and 28.60º for CeO_2 (220): $D=(K\lambda/\beta Cos\Theta)$, where λ is the X-ray wavelength, β is the full width of the diffraction line at half maximum (FWHM), and ϴ is the Bragg angle.

CO-Chemisorption was performed on a chemisorption analyzer (Autochem HP-Micromeritics). Before measurements, samples (ca. 50 mg) were reduced using 50 $NmL \cdot min^{-1}$ in a 12 vol.% H_2/Ar flow at 500 °C for 3 h and a heating ramp of 1 $°C \cdot min^{-1}$. Then, CO-Chemisorption was measured at 35 °C under a 10 vol.% CO/He flow. CO pulses were periodically introduced until saturation was reached. Nickel metal surface area and dispersion were calculated assuming the stoichiometric factor for CO to Ni equal to unity, atomic weight of 58.71, atomic cross-sectional area of 0.0649 nm^2 and density of 8.90 $g \cdot cm^{-3}$. The fresh sample was measured after calcination and after a reduction in a tubular furnace using 100 $NmL \cdot min^{-1}$ in a 5 vol.% H_2/Ar flow at 500 °C for 3 h with a heating and cooling ramp of 1 $°C \cdot min^{-1}$.

Bruker-Alpha FTIR spectrometer (Bruker Optic GmbH, Ettlingen, Germany) in attenuated total reflectance (ATR) configuration was used to obtain ATR-FTIR spectra. Prior to the measurements, each catalyst was crushed, dispersed in isopropanol and deposited directly on the diamond crystal plate. After the solvent evaporation, spectra were collected at room temperature in the range between 375-4000 cm^{-1} with a resolution of 4 cm^{-1} and accumulating 24 scans. Background spectrums were previously acquired without the samples and automatically subtracted from the samples spectra. The processing of FTIR data was performed using Bruker OPUS spectroscopy software.

SEM imaging, mapping and elemental composition analysis were conducted at 20 kV using a scanning electron microscope (SU-70 Hitachi) equipped with an energy dispersive X-rays spectroscopy detector (EDX, Oxford Instruments). The as-received catalyst samples from the reactors were gently crushed prior to SEM-EDX analysis to better observe the inner parts of the used catalyst. No coating was necessary since the samples are of conductive nature. The chemical composition analysis was restricted to Ni, Al, Ce, O and S, and it was computed as the average over ten measurements on different regions for each powder sample. A copper standard was used for the system calibration.

TEM and HRTEM analysis were carried out using a using a Philips Tecnai F20 field emission microscope, 200 kV and 45 μA, equipped with a Gatan Ultrascan CMOS camera and EDAX energy dispersive spectrometer for chemical analysis. The powder samples were crushed in an agate mortar and the solid particles dispersed in isopropanol (~10mL) using an ultrasonic bath. Two or three drops of the nanoparticles suspension were deposited on a holey carbon-coated copper grid (300 mesh, Agar Scientific Ltd., Essex, UK) and then dried at room conditions. The samples preparation was carried out rapidly to minimize their possible oxidation caused by their contact with the environment. The size distribution of the metallic particles supported on Al_2O_3 were built by independent image analysis of approximately 720-1100 particles for each solid sample using the Gatan Digital Micrograph software. The obtained electron diffraction patterns were radially integrated using Gwyddion.

3. Results and Discussion

3.1. Catalytic performance

The CO_2 methanation was carried out using biogas from sewage sludge anaerobic digestion and electrolytic hydrogen as feedstock. After conditioning, the gases reacted over a nickel-ceria-based catalyst to produce synthetic natural gas in two-reactors in series, with intermediate water removal to shift chemical equilibrium towards methane and the inhibiting effect on the reaction kinetics [44]. As an average, the gas composition after the first reactor was 83.65% CH_4, 13.18% H_2 and 3.17% CO_2. The synthetic natural gas quality was successfully upgraded after the second reactor to 95.52% CH_4, 3.35% H_2 and 1.13% CO_2. Figure *3* shows the evolution of the gas composition during the long-term experiment of 1,000 hours. As presented, a slight dispersion of the composition values was observed, especially after 400 hours on-stream, which arose from small flow variations of the inlet composition and the gas controllers. As a general rule, the overall picture suggest that the gas composition did not show any specific trend over time. Therefore, it can be stated that uniform gas quality was obtained during the whole experimental campaign.

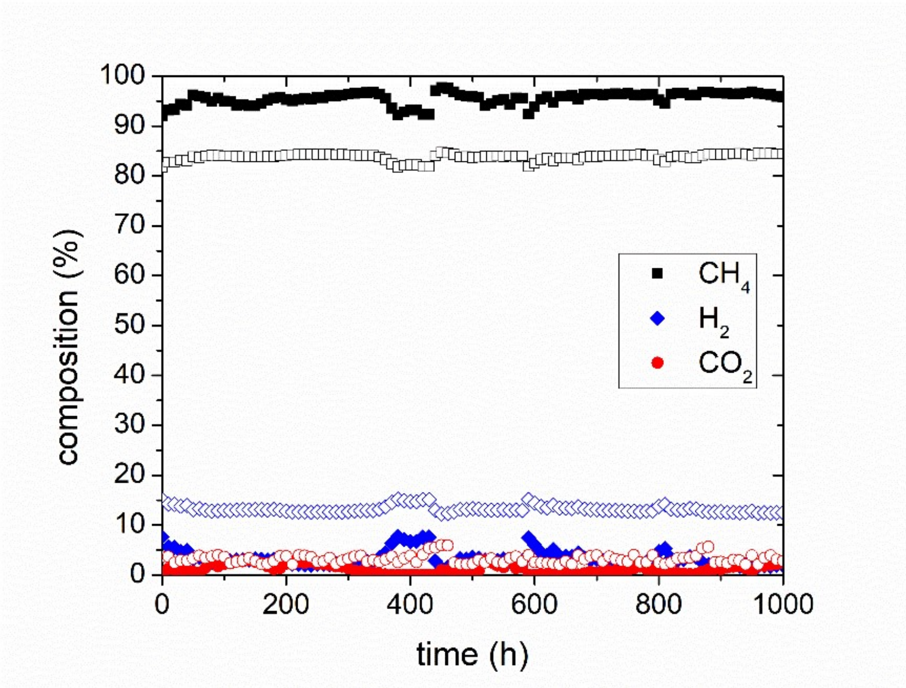

Figure *3*. Composition after reactor 1 (hollow symbols) and after reactor 2 (filled symbols).

The reactors operated non-isothermally in decreasing temperature profile on a compromise between kinetics and equilibrium limitations. Figure *4* shows the temperature profiles during the 6 weeks (W1-W6) of continuous time-on-stream. Despite some alterations, the temperature profiles did not change during the six weeks of operation, suggesting that still active catalyst was present at all sections.

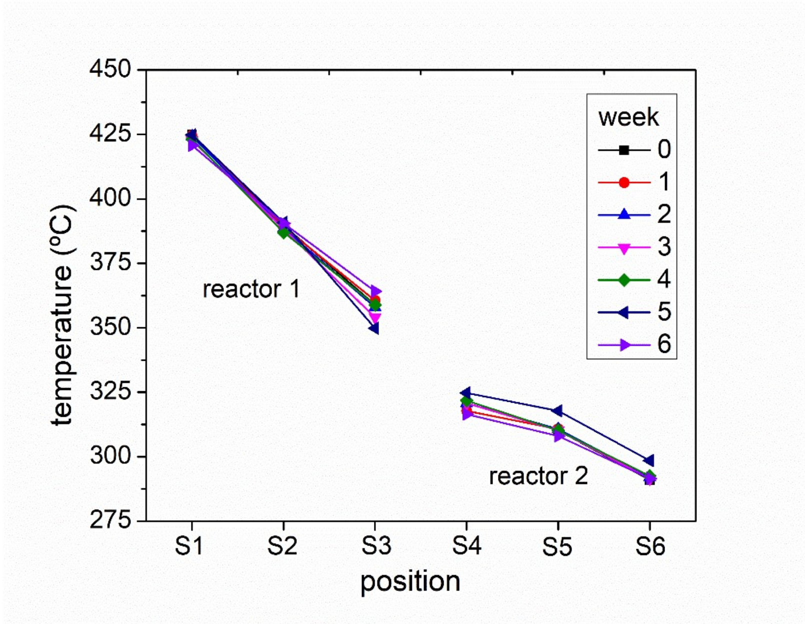

Figure *4*. Evolution of reaction temperature profiles over the weeks (W0-W6).

As the reaction extent increases, temperatures and gas composition varied significantly along the longitudinal profiles of the two reactors in series. In this sense, each catalyst sample (S1-S6) operated at significantly different reaction environments in terms of temperature and gas composition. Table *2* shows an average of the measured temperatures and the gas composition at each reactor zone. The partial pressure of the reactants, hydrogen and carbon dioxide, decreased along the reactor; while that of methane followed an opposite trend. The highest amount of water inside the reactor was attained at the end of each reactor, and most notably, at the end of the first reactor. The significant decrease of the water pressure between reactors is due to the water removal step, between S3 and S4 positions, which allows for shifting the chemical equilibrium. Generally speaking, the gas composition at the end of the first reactor consisted basically on water, followed by methane. Noteworthy, the catalyst behavior at these conditions is rarely studied in the literature.

Table *2*. Estimated operating conditions of the catalyst samples.

sample	T [ºC]	partial pressure [bar]

		P_{H2}	P_{CO2}	P_{CH4}	P_{H2O}
S1	424	3.21	0.80	0.99	0.00
S2	389	-	-	-	-
S3	358	0.29	0.07	1.84	2.80
S4	320	0.64	0.15	4.09	0.12
S5	311	-	-	-	-
S6	293	0.14	0.05	3.86	0.96

3.2. Characterization of catalyst samples from different reaction sections

Table *3* describes the main physicochemical properties of the fresh and spent catalyst samples, in terms of surface area, metallic area, metallic particle diameter and sulphur content as obtained from the different characterization techniques performed. At first glance, it can be seen that some physicochemical properties were clearly affected after utilization in the methanation plant, as opposed to the stable catalytic performance observed. The most remarkable fact was the detection of sulfur in all the used samples, despite the efforts on biogas pre-cleaning process. As a general rule, sulfur was randomly detected in all spent samples (~0.5%). Specifically, the highest concentration (0.91 wt.%) was found at the end of the first reactor; although it is difficult to infer a clear trend on the sulphur content among samples from this analysis. As it will be further discussed, the sulfur presence was confirmed by HRTEM and FTIR.

Table *3*. Main properties of fresh and spent catalysts.

variable	sulphur	surface area	d_{Ni}	d_{CeO2}	$d_{metallic}$	metallic area
technique	EDX	N_2-sorption	XRD	XRD	TEM-PSD	CO-chemi
unit	[wt. %]	[m^2/g]	[nm]	[nm]	[nm]	[m^2/g]
fresh[a]	ND	123	15.45	6.63	14.88	1.72
S1	0.52	98	18.54	7.35	19.56	1.33

S2	0.25	109	15.50	6.88	-	1.31
S3	0.91	106	15.46	6.91	14.61	1.55
S4	0.32	115	15.42	6.87	17.17	1.59
S5	0.49	123	15.44	6.73	-	2.03
S6	0.60	125	15.40	6.78	18.82	1.83

[a] in reduced form

Figure 5 shows an example of a SEM image, the EDX spectra and the elemental mapping of the used catalyst from the section S2, being also representative of the rest of zones assessed (see Figures S1-S5 in the Supporting Information). Apart from the catalyst elemental constituents that are homogeneously dispersed, the presence of evenly distributed S over the catalyst surface is clearly observed in all the samples. At this point, it is evident that some sulfur molecules passed through the sulfur removal filters, being thus undetected by the analytical equipment and, at some point during the operation, contaminated the catalyst.

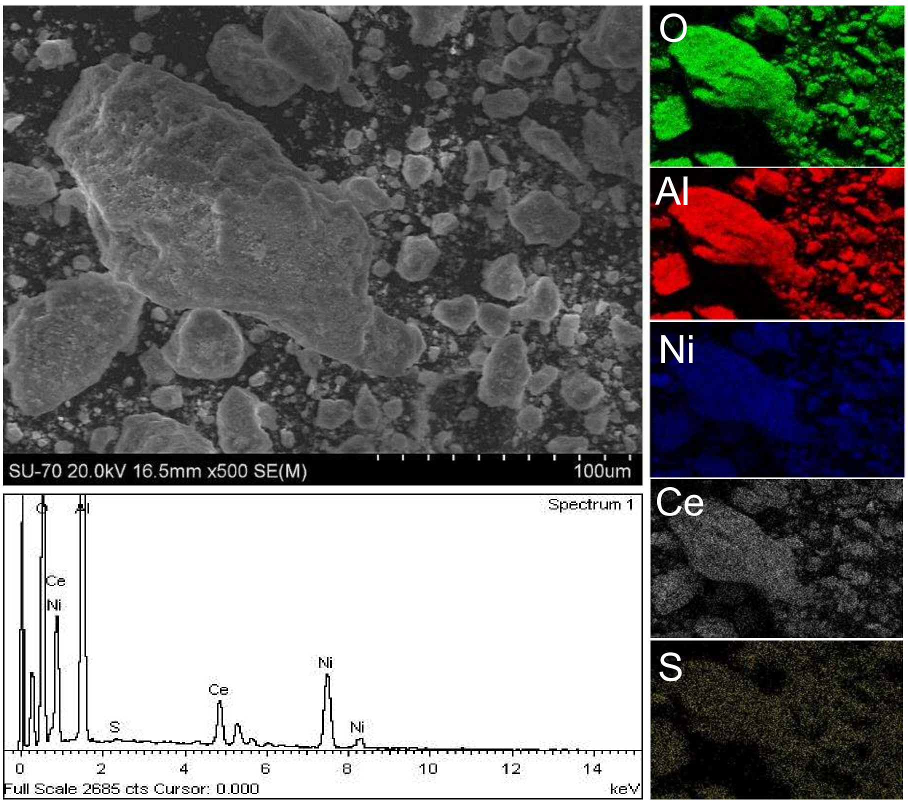

Figure 5. SEM image and EDX elemental mapping of S2 catalyst sample.

The initial BET surface area of the fresh catalyst was 123 m^2/g and after the experimental campaign, the samples located closest to the reactor entrance lost significant surface area. The maximum loss was exhibited in S1 (~20%), e.g. the first reactor inlet, whereas the surface area of S5-S6 samples, e.g. closer to the second reactor outlet, remained unaltered. Accordingly, the following trend can be inferred: the closer the catalyst to the reactor entrance and hence the higher the temperature, the more significant the loss of surface area.

In general, various techniques coincided on that the size of metallic particles was slightly affected by the reaction. In addition to surface area by N_2-physisorption, the sintering of active sites, i.e. nickel nanoparticles, was inferred by XRD, TEM-PSD and CO-chemisorption techniques. More particularly, XRD results from section S1 indicate some sintering of nickel particles at the first reaction zone; about a 15% increase in crystallite size. That is to say that nickel sintering was restricted to the initial zones of the first reactor, in turn related to the highest operation temperatures (T≥450 ºC). The results also suggest a faint sintering behaviour of CeO_2 particles, which can be associated with the structural conversion of non-stochiometric CeO_{2-x} caused by the redox reaction between Ce^{3+} and Ce^{4+} [45]. On the other hand, the inhibition of Ni particles sintering at the reactor outlet can be explained by incorporation of Ni^{2+} species into the lattice of CeO_2 particles [46] and the migration of partially reduced CeO_{2-x} to Ni nanoparticles [47] that generate strong metal-promoter bounding between Ni and CeO_2 nanoparticles [48]. The XRD diffractograms can be found in the Supporting Information (Figure S6-S7).

Figure 6 shows examples of the TEM images collected for the samples from different reactors zones. Individual analysis of multiple TEM images and more than 700 particles for each sample allowed for a proper characterization to build statistically significant particle size distributions (PSD). As presented in Table *3*, the mean metallic particle size of the fresh sample was 14.88 nm and some sintering was particularly evidenced at the initial zones of the reactor. Noteworthy, the distributions are referred to the main spotty particle size of metals and, in all the cases, the PSD showed a unimodal distribution, confirming the slightly bigger particle size for the catalyst located in the S1 zone, in agreement with XRD results. The PSD for each sample obtained from TEM imaging can be found in the Supporting Information (Figure S8).

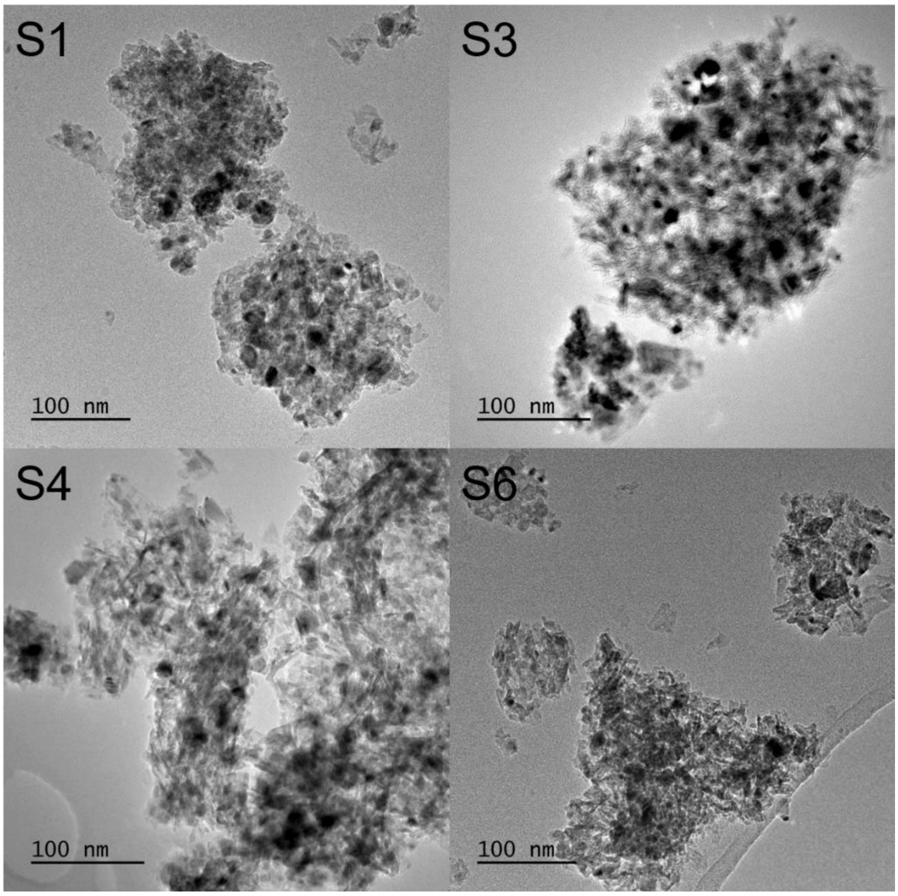

Figure *6.* Examples of TEM images taken for samples in zones S1, S3, S4 and S6 at 38 kX of magnification. Scale bars refer to 100 nm.

CO chemisorption measurements offer a general overview of the nickel dispersion in the support. As a general rule, nickel dispersion is affected by both the availability of surface area and the proper dispersion of nickel active sites [43]. As Table *3* presents, the fresh catalyst exhibited a metallic area of 1.72 m^2/g, which dropped to 1.31-1.33 m^2/g in S1-S2 samples. This reduction of metallic area represents a significant -24%, at the first reactor section after operation with respect to the fresh sample. On the contrary, the samples located at the end of the second reactor exhibited comparable, or even slightly higher metallic values (+12%) if compared to the fresh catalyst. The overall picture suggests that there is a certain tendency to lose metallic area for the catalyst samples that operated at higher temperatures. In agreement with XRD and TEM results, this pattern can be related to the size increase of metallic particles.

The analysis of the electron diffraction patterns of several HRTEM images can provide a rough quantitative approximation of the different metallic species present on the catalyst surface. Approximately 10 images at high magnification were evaluated for each sample and the global analysis of the diffraction patterns revealed that Ni, CeO_2 and Ce_2O_2S were always present in all the sections studied. Noteworthy, the presence of metallic Ni and CeO_2 is fundamental to justify the maintained catalyst activity observed during the experimental campaign. As illustrative examples, Figure 7 and 8 show detailed HRTEM imaging analysis of samples located from very different reactor sections; S1 (inlet of the first reactor) and S6 (outlet of the second), respectively; along with their Fast Fourier Transform (FFT) and the close up identification of the observed Fresnel fringes. Further images of the samples located at the rest of reactors sections can be found in the Supporting Information (Figures S9-S11).

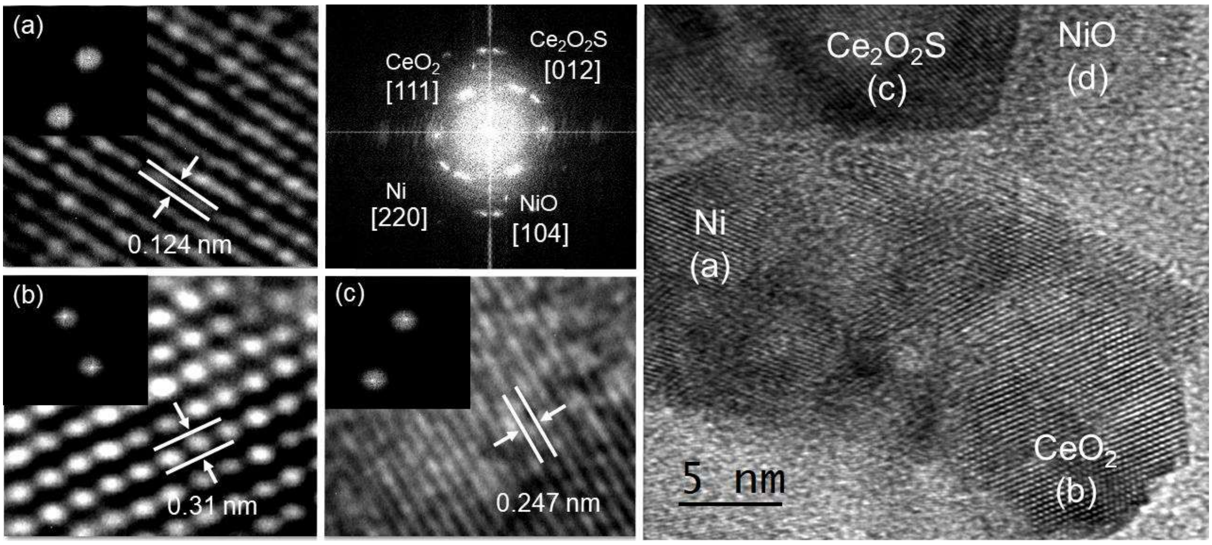

Figure 7. HRTEM image of S1 (first reactor inlet) catalyst at 590 kX of magnification along with the fast Fourier transform. Scale bars refer to 5 nm.

Lattice-fringe and FFT analysis allowed for identifying spots at 0.124 and 0.176 nm that can be related to the characteristic d-spacing of the faces [2 2 0] and [2 0 0] of Ni; while at 0.147 nm was related to [1 0 4] faces of NiO. As for CeO_2, spots at 0.312 and 0.163 nm can be related to the characteristic d-spacing of the faces [1 1 1] and [3 1 1]. Interestingly, the d-spacing at about 0.27 nm, which is related to the face [0 0 2] of NiS, was not generally detected and there is only clear evidence of this phase in two HRTEM images from the section S4 (see Figures S9 and S10, Supporting Information). The main finding from such analysis is that diffraction spots with lattice distances of 0.243 and 0.309 nm, specific for the faces [0 1 2] and [1 0 1] of cerium oxide sulphide (Ce_2O_2S), were identified in several HRTEM images for the samples evaluated from all reactors sections.

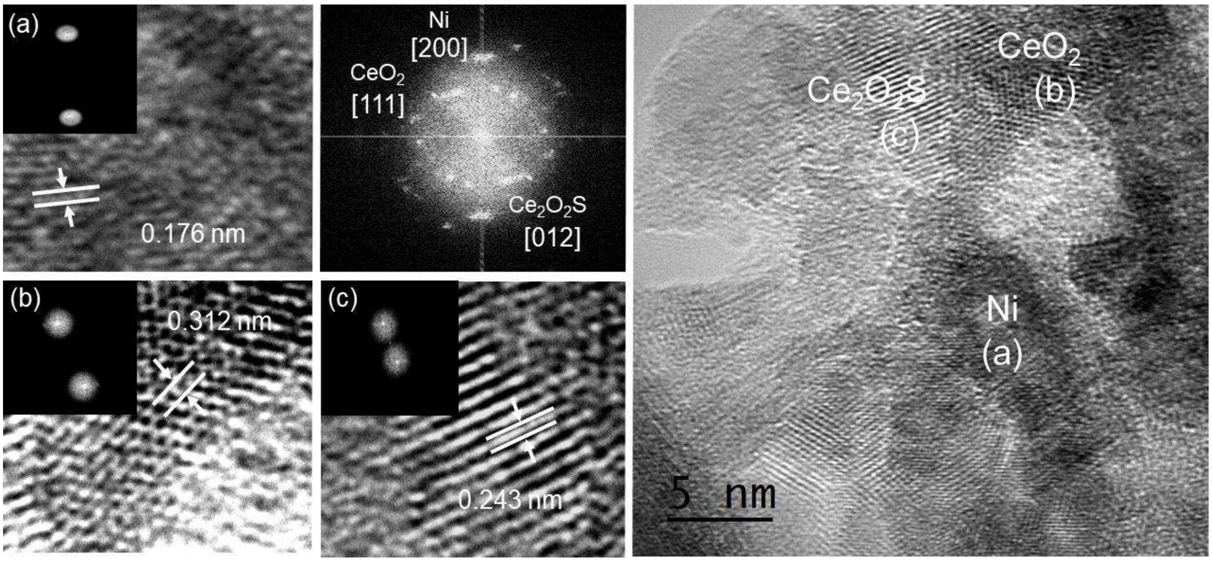

Figure 8. HRTEM image of S6 (second reactor outlet) catalyst at 590 kX of magnification along with the fast Fourier transform. Scale bars refer to 5 nm.

The identification of the chemical species present on the surface of the used catalyst samples was also corroborated by a more detailed analysis through the radial integration of the FFT of several images for the catalyst samples from different zones. Figure 9 shows an example of such an analysis for the section S1. The analogous analysis for the samples from sections S3, S4 and S6 can be found in the Supporting Information Figures S11-S13. As it can be seen, the presence Ce_2O_2S was confirmed by the identification of d-spacings associated with different crystallographic planes, namely [0 0 2], [0 1 2], [1 0 1], [1 0 0], [1 0 3], [1 1 3], [1 1 5], and [2 0 2], in all the reactor zones evaluated. This evidence confirms the paramount role of CeO_2 as sacrificial agent to prevent the poisoning of Ni active sites and the usefulness of the promoter to prevent deactivation across the longitudinal profiles of both reactors. Moreover, the presence of Ni active phase was also confirmed in all the reactors sections studied by the identification of the crystallographic planes [2 0 0], [3 3 1] and [4 2 2], which explains the unchanged catalytic activity after the experimental campaign. Only in few samples, the presence of species derived from the interaction between Ni and S were observed, yet the identification was not fully discriminative given the similarity between the lattice spacing of other species. They were namely related to the phases NiS and Ni_3S_2. This is another evidence of the crucial function of CeO_2 in the catalyst formulation to prevent the poisoning of the actual active sites.

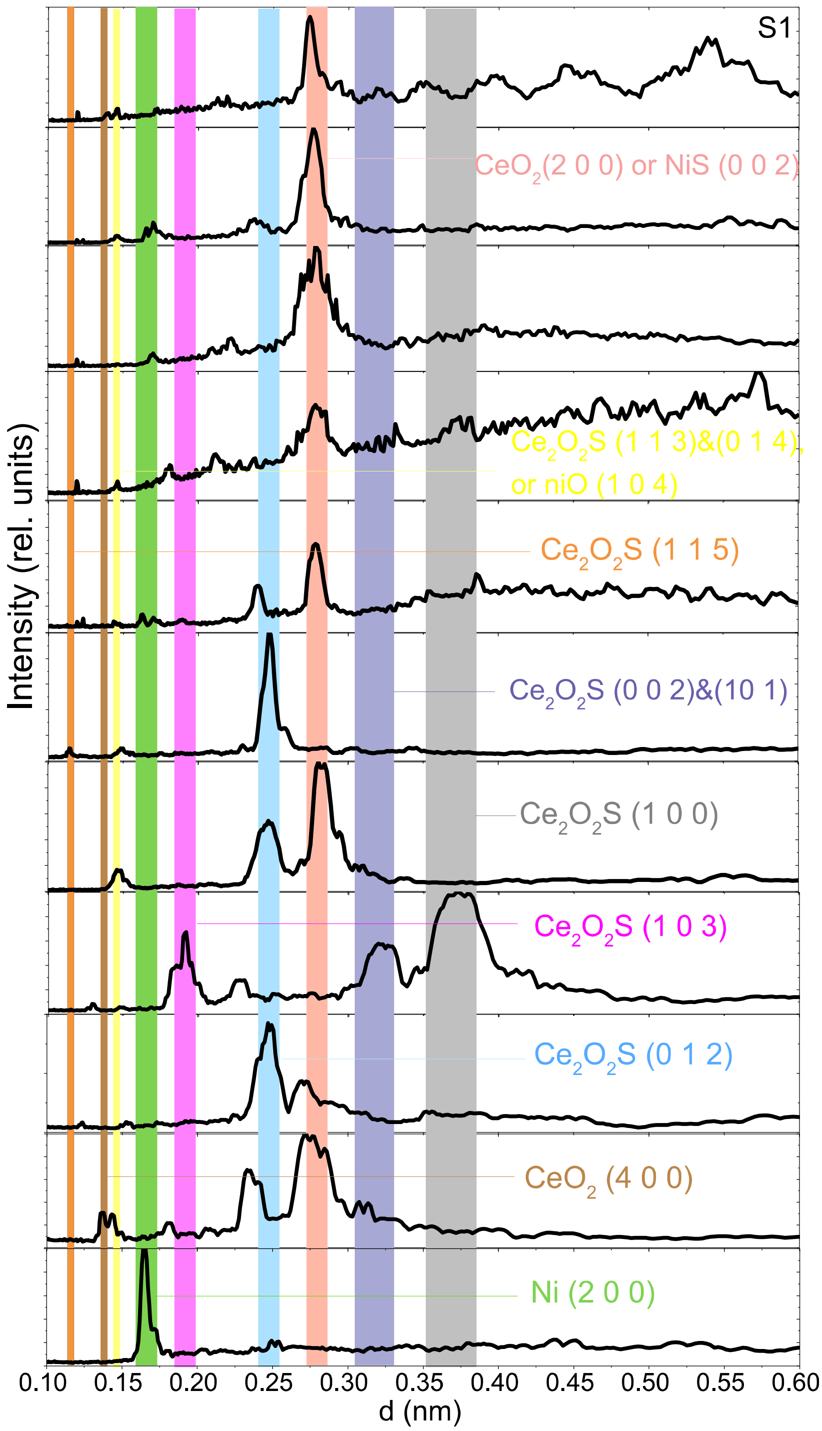

Figure 9. Electron diffraction patterns obtained by radial integration of the TEM fast Fourier transforms of several catalyst samples from S1 section.

For further inspection of the surface chemistry of the fresh and used catalyst samples (S1-S6), ATR-FTIR spectroscopy measurements were performed at room temperature. The corresponding FTIR spectra are reported in Figure 10. The broad band located at 3345 cm^{-1} was assigned to hydroxyl groups (O-H stretching vibrations), while the weak peak at 1650 cm^{-1} was attributed to adsorbed water (H-O-H bending vibrations mode). Regarding the peaks of metal-oxygen vibration modes, the Ni-O stretching at 720 cm^{-1} and the O-Ce-O stretching at 485 cm^{-1} were identified [49] . Compared to the fresh catalyst, two new bands at 1160 and 1105 cm^{-1} were identified for the samples exposed to reactions conditions. They were assigned to $(SO_4)^{2-}$ stretching vibration mode. It is important to note that the intensity of these bands were more pronounced for the samples S4-S6, which were located at the second reactor. Therefore, the presence of sulphur derivatives in the spent sample was also detected by FTIR data, in concordance with SEM-EDX and HRTEM analysis.

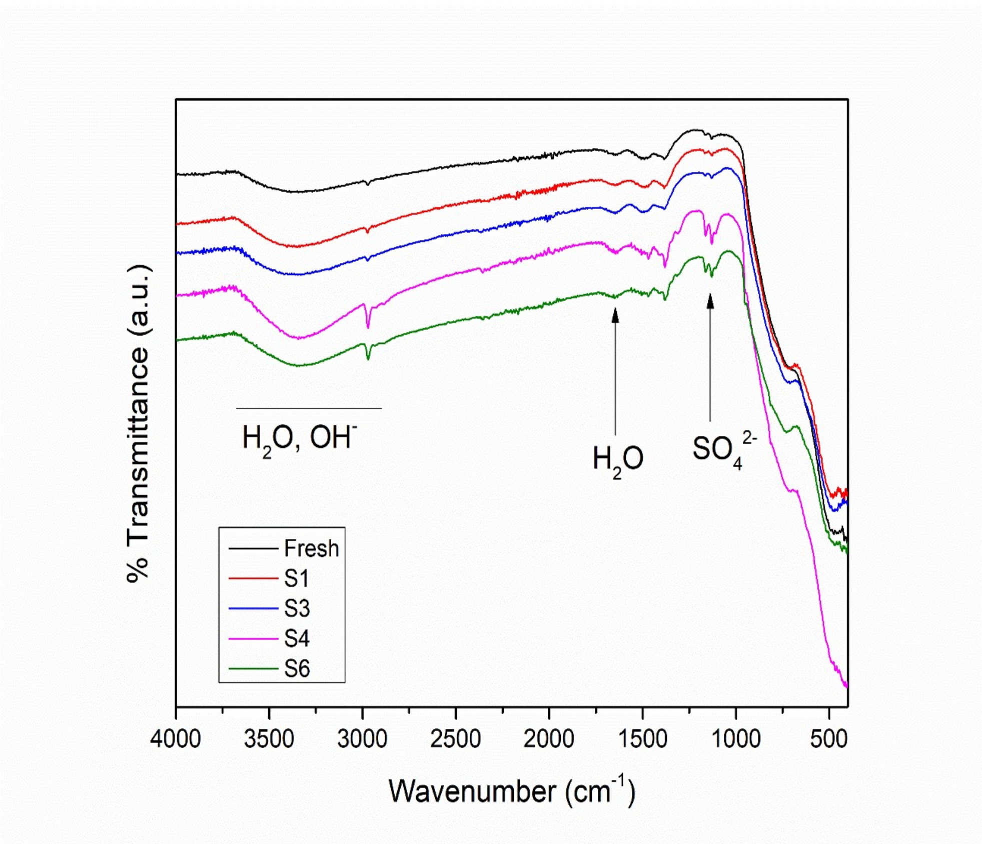

Figure 10. FTIR spectra of the fresh and spent samples collected in the wavenumber range of 400-4000 cm^{-1}.

3.3. Discussion

The characterization of the catalyst samples from different reactors zones unravelled valuable information to understand the catalytic performance otherwise masked by simple assessment of the catalytic activity in terms of the product distribution determined by micro-chromatography. On one hand, XRD and the PSD obtained from TEM imaging agree that sintering is at play to some extent in the beginning of the first reactor, as it can be inferred from the larger metallic particle size estimated from both techniques. This fact is also in coherence with the observed loss of surface area in S1 determined by N_2-physisorption and with the loss of metallic surface area determined by CO-chemisorption. The most plausible explanation for such sintering, particularly pronounced for Ni particles, relies on the higher temperature of the S1 zone T~425 °C, including punctual temperatures of T~450ºC during operation, being sufficient to trigger sintering of Ni but unlikely enough to initiate that of Ce particles, in agreement with previous findings in the literature [50,51]. On the other hand, SEM-EDX, lattice-fringes analysis of HRTEM images and the radial integration of the FFT, along with FTIR, confirm the presence of sulphur derivatives across the whole longitudinal section of both reactors. This finding was somewhat unexpected yet is of paramount relevance since it reveals that although intensive efforts were devoted towards sulphur removal and monitoring, poison molecules are able to reach the reactors. In this sense, this fact reinforces the importance of taking not only upstream precautions to avoid the catalyst deactivation, but also to implement protective measures in the catalyst formulation. Accordingly, the use of CeO_2 as promoter proved its utility to enhance the catalyst tolerance to sulphur poisoning, as confirmed by the consistent presence of Ce_2O_2S along the reactor and the presence of Ni active phase after the experimental campaign determined by HRTEM.

The interaction of H_2S, coming with the biogas used to feed the reactor, with nickel involves multiple fundamental steps. The structure and stoichiometry of sulfur adsorbed on nickel is function of temperature and H_2S concentration [52]. The saturation coverage of the fast, exothermic, reversible sulfur chemisorption on nickel surface is about 17 μmol S/m^2 Ni [53], which for the present catalyst corresponds to 0.1 wt.% of S. At typical methanation temperatures, McCarty et al. found that 0.7 ppb H_2S led to 90% of saturation coverage by means of sulfur chemisorption [23]. Besides, they expressed that regeneration by hydrogen reduction is impractical due to low equilibrium partial pressure of H_2S. Therefore, further migration of S into the bulk and formation of Ni_xS_y stable phases seem plausible, e.g. Ni_3S_2 phase. Nonetheless, very stable Ni_xS_y phases were not present in the spent samples; in contrast to Gaikwad et al., which operated in real conditions using an unpromoted Ni-based methanation catalyst [37]. The present catalytic system was composed of Ni-Ce/Al_2O_3 ternary system and therefore, the sacrificial role of the promoter plays a paramount role to prevent the poisoning of Ni active sites. Indeed, CeO_2 has high affinity for H_2S (Equation 2). Although sulfur poisoning on Ni is possible, Silva et al. [54] found that the incorporation of CeO_2 on Ni-based catalyst thermodynamically reduce the sulfur chemisorption on Ni by lowering the sulfur chemical potential. Thus, ceria acts as sulfur sorbent for biogas to form Ce_2O_2S, which eventually leads to an enhanced tolerance of the catalyst formulation to sulphur poisoning.

$$H_2S\ (g) + 2\ CeO_2 \leftrightarrow Ce_2O_2S\ (s) + 2\ H_2\ (g) \qquad \text{(Equation 2)}$$

Ceria sulfurization is thermodynamically favoured at low temperature and high H_2S concentrations [55]. Catalyst samples located at the entrance of the reaction unit (e.g. S1) are, in principle, more prone to sulfurization because they are exposed to higher H_2S concentration coming from the biogas stream. Nevertheless, not all the sulfur that entered the reactor was adsorbed in the first reactor zones. Indeed, the latest catalyst zones of each reactor (S3 and S6) showed higher amount of sulfur. These two reactor zones have in common a lower temperature and the presence of higher water content. Sulfur poisoning of nickel and ceria involve the formation of a complex set of compounds. This complexity can be observed by considering Ni-O-S and Ce-O-S phase diagrams [56]. Under oxidizing conditions, sulfur reacts with ceria to form cerium sulphates and metallic nickel with oxygen to oxidized form [57]. These oxidative reactions could take place in the second reactor; in punctual situations where the hydrogen could be exhausted and the presence of H_2O leads to oxygen partial pressure higher than 10^{-20} bar, causing instability of the metal sulphides. Indeed, the ATR-FTIR spectra of the used catalyst revealed the stretching modes of sulphate ion (1160 and 1105 cm^{-1}) and water (broad band 2600-3000 cm^{-1}) together with its bending vibration (1667 cm^{-1}) [58], being more pronounced in the second reactor. In this regard, it can be inferred that is important to maintain a certain residual hydrogen concentration in the gas outlet.

The continuous monitoring of the biogas by micro-chromatography assured that the amount of H_2S entering the system was below 3 ppm and external analytics confirmed that the amount of sulfur was below 22 ppb during gas sampling. In this regard, the two active carbon filters and the ZnO adsorbent, which were implemented in series, apparently worked successfully. Unavoidably, some sulfur molecules definitely were able to enter to the reactor. Very few sulfur molecules (≤ 22 ppb) could be present in the biogas during the whole experimental campaign. Another possibility is that, at some point, a peak of sulfur content (≤ 3 ppm) entered to the reactor and it was not detected by the in-situ analytics.

Plug flow poisoning is caused by a strong poison, which results in the deactivation moving as a progressive front from the point of impingement throughout the catalyst bed. This deactivation mechanism is not deemed feasible since the temperature profile was not accordingly shifted towards the reactor end. In contrast, diffuse flow poisoning arising from the formation of stable nickel and ceria sulphides across the whole reactor longitudinal profile is a more plausible mechanism to govern because sulfur was detected in the different sections of the reactors evaluated. In this line, very low concentration of sulfur contaminants acted as diffusional deactivators, in contrast to plug flow poisoning, as for instance occur in other reactions [59]. Catalyst deactivation by poisoning was not evidenced during the experimental campaign due to the prevention actions and that, at these high flow rates, mass transfer may have controlled the reaction [31]. From these findings, apart from an adequate filtration system and the loading of a sulfur-resistant catalyst as cerium, lanthanum oxide [60] or less expensive metal oxides [61]; future industrial methanation plants should incorporate enough tools to correct possible losses of outlet gas quality during the catalyst lifetime. For instance, an increase of the reaction pressure, at least before catalyst replacement, would provide enough flexibility to the process to withstand such drawback.

4. Conclusions

The stability of a nickel/ceria-based catalyst on real biogas methanation to synthetic natural gas was evaluated in a pilot plant for 1,000 hours of uninterrupted operation. The gas quality and temperature profile remained constant during operation, indicating no signs of catalyst deactivation. Catalyst samples were withdrawn separately from each of the six reactor sections evaluated and analyzed by a set of characterization techniques.

The size of metallic nanoparticles, both nickel and ceria, was increased at the first reaction zones (+10-30%), related to the highest operation temperatures. In the rest of the reaction zones (T<450 ºC), the metallic particle diameter remained unaltered, in coherence with the constant catalyst surface area. The most striking finding reveals that sulfur was detected along the entire reaction zones. The concentration of sulphur was higher at the outlet of each reactor (>0.6 wt.%). This finding is related to the Ni-O-S and Ce-O-S phase equilibrium. Under the more oxidizing conditions and lower temperatures at the end of each reactor, sulfur is more prone to react with ceria to form very stable cerium sulphates. The analysis of HRTEM diffraction patterns revealed that Ce_2O_2S was always present, together with Ni and CeO_2, confirming that in real conditions CeO_2 acts as sulfur sorbent for biogas streams.

This work evidenced that sulfur molecules passed through the complete removal system and they were not detected by the analytic equipment. The deactivation mechanism proposed in this work is diffuse flow poisoning by predominantly formation of ceria sulphides and eventually nickel sulphides across the entire profile of the reactors.

Acknowledgements

Authors thank Generalitat de Catalunya for financial support through the CERCA Programme, M2E (2017SGR1246) and XaRMAE network. IREC is gratefully acknowledge the funding of this work by the CoSin project (COMRDI15-1-0037), funded by ACCIÓ and the European Regional Development Fund (ERDF) under the framework of RIS3CAT Energy Community. Authors gratefully thank INERATEC GmbH for supplying the microstructured reactors and for their assistance in the catalyst implementation. We also thank to the industrial partner Naturgy, especially to Ignasi Mallol, to actively collaborate in this demonstration project. Authors kindly thank Dr. Albert Llorente (from IREC) for characterization of samples and Dr. Alan Harvey and Dr. Vasily Lebedev (both from University of Limerick) for their help with the TEM-HRTEM imaging and data analysis.

5. References

[1] Abad AV, Dodds PE. Green hydrogen characterisation initiatives: Definitions, standards, guarantees of origin, and challenges. Energy Policy 2020;138:111300.

[2] Abe JO, Popoola API, Ajenifuja E, Popoola OM. Hydrogen energy, economy and storage: review and recommendation. Int J Hydrogen Energy 2019;44:15072–86.

[3] IEA. The future of hydrogen. Paris: 2019.

[4] IRENA. Hydrogen: A renewable energy perspective. 2019.

[5] Schildhauer TJ, Biollaz SMA. Synthetic Natural Gas: From Coal, Dry Biomass, and Power-to-Gas Applications. John Wiley & Sons; 2016.

[6] Becker WL, Penev M, Braun RJ. Production of synthetic natural gas from carbon dioxide and renewably generated hydrogen: a techno-economic analysis of a power-to-gas strategy. J Energy Resour Technol 2019;141.

[7] Daiyan R, MacGill I, Amal R. Opportunities and Challenges for Renewable Power-to-X. ACS Energy Lett 2020;5:3843–3847.

[8] Guilera J, Ramon Morante J, Andreu T. Economic viability of SNG production from power and CO2. Energy Convers Manag 2018;162:218–24. https://doi.org/https://doi.org/10.1016/j.enconman.2018.02.037.

[9] Walker SB, Sun D, Kidon D, Siddiqui A, Kuner A, Fowler M, et al. Upgrading biogas produced at dairy farms into renewable natural gas by methanation. Int J Energy Res 2018;42:1714–28.

[10] Frontera P, Macario A, Ferraro M, Antonucci P. Supported Catalysts for CO2 Methanation: A Review. Catalysts 2017;7:59. https://doi.org/10.3390/catal7020059.

[11] Ashok J, Pati S, Hongmanorom P, Tianxi Z, Junmei C, Kawi S. A review of recent catalyst advances in CO2 methanation processes. Catal Today 2020;356:471–89. https://doi.org/https://doi.org/10.1016/j.cattod.2020.07.023.

[12] Bartholomew CH. Mechanisms of catalyst deactivation. Appl Catal A Gen 2001;212:17–60. https://doi.org/https://doi.org/10.1016/S0926-860X(00)00843-7.

[13] Ewald S, Kolbeck M, Kratky T, Wolf M, Hinrichsen O. On the deactivation of Ni-Al catalysts in CO2 methanation. Appl Catal A Gen 2018. https://doi.org/https://doi.org/10.1016/j.apcata.2018.10.033.

[14] Mebrahtu C, Perathoner S, Giorgianni G, Chen S, Centi G, Krebs F, et al. Deactivation mechanism of hydrotalcite-derived Ni–AlOx catalysts during low-temperature CO2 methanation via Ni-hydroxide formation and the role of Fe in limiting this effect. Catal Sci Technol 2019;9:4023–35. https://doi.org/10.1039/C9CY00744J.

[15] Mutz B, Carvalho HWP, Mangold S, Kleist W, Grunwaldt J-D. Methanation of CO2:

Structural response of a Ni-based catalyst under fluctuating reaction conditions unraveled by operando spectroscopy. J Catal 2015;327:48–53.

[16] Mutz B, Gänzler AM, Nachtegaal M, Müller O, Frahm R, Kleist W, et al. Surface oxidation of supported Ni particles and its impact on the catalytic performance during dynamically operated methanation of CO2. Catalysts 2017;7:279.

[17] Koschany F, Schlereth D, Hinrichsen O. On the kinetics of the methanation of carbon dioxide on coprecipitated NiAl (O) x. Appl Catal B Environ 2016;181:504–16.

[18] Abelló S, Berrueco C, Montané D. High-loaded nickel–alumina catalyst for direct CO2 hydrogenation into synthetic natural gas (SNG). Fuel 2013;113:598–609. https://doi.org/http://dx.doi.org/10.1016/j.fuel.2013.06.012.

[19] Alrafei B, Polaert I, Ledoux A, Azzolina-Jury F. Remarkably stable and efficient Ni and Ni-Co catalysts for CO2 methanation. Catal Today 2020;346:23–33.

[20] Müller K, Fleige M, Rachow F, Schmeißer D. Sabatier based CO2-methanation of Flue Gas Emitted by Conventional Power Plants. Energy Procedia 2013;40:240–8. https://doi.org/https://doi.org/10.1016/j.egypro.2013.08.028.

[21] Moulijn JA, Van Diepen AE, Kapteijn F. Catalyst deactivation: is it predictable?: What to do? Appl Catal A Gen 2001;212:3–16.

[22] Hakawati R, Smyth BM, McCullough G, De Rosa F, Rooney D. What is the most energy efficient route for biogas utilization: heat, electricity or transport? Appl Energy 2017;206:1076–87.

[23] McCarty JG, Wise H. Thermodynamics of sulfur chemisorption on metals. I. Alumina-supported nickel. J Chem Phys 1980;72:6332–7.

[24] Hepola J, Simell P, Kurkela E, Ståhlberg P. Sulphur poisoning of nickel catalysts in

catalytic hot gas cleaning conditions of biomass gasification. Stud. Surf. Sci. Catal., vol. 88, Elsevier; 1994, p. 499–506.

[25] Haldor Topsoe. Promoted zinc oxide absorbent (HTZ-51) 2020. https://www.topsoe.com/products/catalysts/htz-51#.

[26] Clariant. Adsorbent for sulfur removal at high space velocities (ActiSorb® S2) 2020. https://www.clariant.com/es/Solutions/Products/2019/03/12/10/14/ActiSorb-S-2.

[27] Köchermann J, Schneider J, Matthischke S, Rönsch S. Sorptive H2S removal by impregnated activated carbons for the production of SNG. Fuel Process Technol 2015;138:37–41.

[28] Agilent Technologies. Detection of Sulfur Compounds in Natural Gas According to ASTM D5504 with an Agilent Dual Plasma Sulfur Chemiluminescence Detector. 2016.

[29] Wolf M, Wong LH, Schüler C, Hinrichsen O. CO2 methanation on transition-metal-promoted Ni-Al catalysts: Sulfur poisoning and the role of CO2 adsorption capacity for catalyst activity. J CO2 Util 2020;36:276–87. https://doi.org/10.1016/j.jcou.2019.10.014.

[30] Vicente J, Montero C, Ereña J, Azkoiti MJ, Bilbao J, Gayubo AG. Coke deactivation of Ni and Co catalysts in ethanol steam reforming at mild temperatures in a fluidized bed reactor. Int J Hydrogen Energy 2014;39:12586–96.

[31] Alarcón A, Guilera J, Soto R, Andreu T. Higher tolerance to sulfur poisoning in CO2 methanation by the presence of CeO2. Appl Catal B Environ 2020;263:118346. https://doi.org/10.1016/j.apcatb.2019.118346.

[32] Rabe S, Vogel F, Truong T-B, Shimazu T, Wakasugi T, Aoki H, et al. Catalytic reforming of gasoline to hydrogen: Kinetic investigation of deactivation processes. Int

J Hydrogen Energy 2009;34:8023–33.

[33] Ivanov KI, Dimitrov DY. Deactivation of an industrial iron-molybdate catalyst for methanol oxidation. Catal Today 2010;154:250–5.

[34] Wolf M, Schüler C, Hinrichsen O. Sulfur poisoning of co-precipitated Ni–Al catalysts for the methanation of CO2. J CO2 Util 2019;32:80–91. https://doi.org/https://doi.org/10.1016/j.jcou.2019.03.003.

[35] Dannesboe C, Hansen JB, Johannsen I. Removal of sulfur contaminants from biogas to enable direct catalytic methanation. Biomass Convers Biorefinery 2019:1–12.

[36] Dannesboe C, Hansen JB, Johannsen I. Catalytic methanation of CO 2 in biogas: experimental results from a reactor at full scale. React Chem Eng 2020;5:183–9.

[37] Gaikwad R, Villadsen SNB, Rasmussen JP, Grumsen FB, Nielsen LP, Gildert G, et al. Container-Sized CO2 to Methane: Design, Construction and Catalytic Tests Using Raw Biogas to Biomethane. Catalysts 2020;10:1428.

[38] Guilera J, Andreu T, Basset N, Boeltken T, Timm F, Mallol I, et al. Synthetic natural gas production from biogas in a waste water treatment plant. Renew Energy 2020;146:1301–8. https://doi.org/https://doi.org/10.1016/j.renene.2019.07.044.

[39] Ingeniería Analítica. Biogas and Natural Gas (Analytical Services) n.d. http://www.ingenieria-analitica.com/servicios-analiticos/petroquimica-y-energia/biogas-y-gas-natural.html.

[40] Peter Pfeifer; Michael Belimov. WO2017211864 (A1) Micro-reactor and method implementation for methanation, 2017.

[41] Guilera J, Boeltken T, Timm F, Mallol I, Alarcón A, Andreu T. Pushing the limits of SNG process intensification: high GHSV operation at pilot scale. ACS Sustain Chem

Eng 2020;8:8409–18.

[42] Alarcón A, Guilera J, Andreu T. An insight into the heat-management for the CO2 methanation based on free convection. Fuel Process Technol 2021;213:106666. https://doi.org/https://doi.org/10.1016/j.fuproc.2020.106666.

[43] Alarcón A, Guilera J, Díaz JA, Andreu T. Optimization of nickel and ceria catalyst content for synthetic natural gas production through CO2 methanation. Fuel Process Technol 2019;193:114–22. https://doi.org/https://doi.org/10.1016/j.fuproc.2019.05.008.

[44] Gutiérrez-Martín F, Rodríguez-Antón LM, Legrand M. Renewable power-to-gas by direct catalytic methanation of biogas. Renew Energy 2020;162:948–59. https://doi.org/https://doi.org/10.1016/j.renene.2020.08.090.

[45] Ozawa M. Effect of oxygen release on the sintering of fine CeO2 powder at low temperature. Scr Mater 2004;50:61–4. https://doi.org/https://doi.org/10.1016/j.scriptamat.2003.09.040.

[46] Wang N, Qian W, Chu W, Wei F. Crystal-plane effect of nanoscale CeO2 on the catalytic performance of Ni/CeO2 catalysts for methane dry reforming. Catal Sci Technol 2016;6:3594–605. https://doi.org/10.1039/C5CY01790D.

[47] Li M, Amari H, van Veen AC. Metal-oxide interaction enhanced CO2 activation in methanation over ceria supported nickel nanocrystallites. Appl Catal B Environ 2018;239:27–35. https://doi.org/https://doi.org/10.1016/j.apcatb.2018.07.074.

[48] Farmer JA, Campbell CT. Ceria maintains smaller metal catalyst particles by strong metal-support bonding. Science (80-) 2010;329:933–6.

[49] Sourisseau C, Fouassier M, Mauricot R, Boucher F, Evain M. Structure and bonding

in cerium oxysulfide compounds. II—Comparative lattice dynamics calculations on Ce2O2S and Ce2.0O2.5S. J Raman Spectrosc 1997;28:973–8. https://doi.org/https://doi.org/10.1002/(SICI)1097-4555(199712)28:12<973::AID-JRS192>3.0.CO;2-F.

[50] Rostrup-Nielsen JR, Pedersen K, Sehested J. High temperature methanation: Sintering and structure sensitivity. Appl Catal A Gen 2007;330:134–8. https://doi.org/https://doi.org/10.1016/j.apcata.2007.07.015.

[51] Ozawa M. Effect of oxygen release on the sintering of fine CeO2 powder at low temperature. Scr Mater 2004;50:61–4. https://doi.org/https://doi.org/10.1016/j.scriptamat.2003.09.040.

[52] Argyle M, Bartholomew C. Heterogeneous Catalyst Deactivation and Regeneration: A Review. Catalysts 2015;5:145–269. https://doi.org/10.3390/catal5010145.

[53] Poels EK, Van Beek WP, Den Hoed W, Visser C. Deactivation of fixed-bed nickel hydrogenation catalysts by sulfur. Fuel 1995;74:1800–5.

[54] Lima da Silva A, Heck NC. Oxide incorporation into Ni-based solid oxide fuel cell anodes for enhanced sulfur tolerance during operation on hydrogen or biogas fuels: A comprehensive thermodynamic study. Int J Hydrogen Energy 2015;40:2334–53. https://doi.org/https://doi.org/10.1016/j.ijhydene.2014.12.037.

[55] da Silva AL, Heck NC. Thermodynamics of sulfur poisoning in solid oxide fuel cells revisited: The effect of H2S concentration, temperature, current density and fuel utilization. J Power Sources 2015;296:92–101. https://doi.org/https://doi.org/10.1016/j.jpowsour.2015.07.046.

[56] Ferrizz RM, Gorte RJ, Vohs JM. Determining the Ce2O2S–CeOx phase boundary for conditions relevant to adsorption and catalysis. Appl Catal B Environ 2003;43:273–80.

https://doi.org/https://doi.org/10.1016/S0926-3373(02)00323-5.

[57] Gong M. Sulfur Tolerant Solid Oxide Fuel Cell for Coal Syngas Application: Experimental Study on Diverse Impurity Effects and Fundamental Modeling of Electrode Kinetics. 2010.

[58] Kathiravan P, Balakrishnan T, Srinath C, Ramamurthi K, Thamotharan S. Growth and characterization of α-nickel sulphate hexahydrate single crystal. Karbala Int J Mod Sci 2016;2:226–38. https://doi.org/https://doi.org/10.1016/j.kijoms.2016.08.002.

[59] Parra D, Izquierdo JF, Cunill F, Tejero J, Fite C, Iborra M, et al. Catalytic activity and deactivation of acidic ion-exchange resins in methyl tert-butyl ether liquid-phase synthesis. Ind Eng Chem Res 1998;37:3575–81.

[60] Dou L, Fu M, Gao Y, Wang L, Yan C, Ma T, et al. Efficient sulfur resistance of Fe, La and Ce doped hierarchically structured catalysts for low-temperature methanation integrated with electric internal heating. Fuel 2021;283:118984. https://doi.org/https://doi.org/10.1016/j.fuel.2020.118984.

[61] Hidalgo-Vivas A, Cooper BH. Sulfur removal methods. Handb Fuel Cells 2010. https://doi.org/https://doi.org/10.1002/9780470974001.f302016.